PAPER

Check for updates

High electrochemical performance of nickel cobaltite@biomass carbon composite (NiCoO@BC) derived from the bark of *Anacardium occidentale* for supercapacitor application†

Modou Diop, [ID] [ab] Baye Modou Ndiaye,[ab] Sokhna Dieng,[b] Balla D. Ngom [ID] *[b] and Mohamed Chaker*[a]

Biomass carbon-based materials are highly promising for supercapacitor (SC) electrodes due to their availability, environment-friendliness, and low cost. Herein, an easy energy-saving hydrothermal process was used to produce $NiCo_2O_4/NiOOH$ (NiCoO) composites with biomass carbon (BC) derived from the bark of *Anacardium occidentale* (AO) at different synthesis time durations (2 h, 4 h, 8 h, 16 h). The structural and morphological properties of the samples were analysed using XRD, Raman spectroscopy, XPS, SEM, TEM and BET, and the results exhibit the presence of carbon inserted into the nickel–cobalt hydroxide matrix. The NiCoO@BC composite synthesized in 4 h (NiCoO@BC(4 h)) displays a good specific capacitance of 475 F g^{-1} at 0.5 A g^{-1} and a low equivalent series resistance (ESR) value of 0.36 Ω. It shows a good coulombic efficiency of 98% and retains 86% of the capacitance after 4000 cycles. The asymmetric supercapacitor (ASC) device (NiCoO@BC(4 h)//AC) assembled using activated carbon (AC) as a negative electrode displays 20 W h kg^{-1} energy density and 900 W kg^{-1} power density at 1 A g^{-1}. The stability test shows a good coulombic efficiency of 99% and 78% capacitance retention after 15 000 cycles. These findings imply that NiCoO@BC composites have outstanding electrochemical properties, making them suitable as SC electrode materials.

1. Introduction

The current energy crisis and the reliance on fossil fuels for production highlight the need for a paradigm shift towards eco-friendly and renewable energy sources. Sunlight and wind are great alternative options.[1] However, these intermittent sources require electrochemical energy storage devices to circumvent discontinuity.[2] Supercapacitors (SCs) are currently considered attractive energy storage devices due to their good stability, low maintenance cost, high power density, and eco-friendliness compared to battery devices.[3–6] SCs may be divided based on the mechanism of energy storage into two main groups:[7] electric double-layer capacitors (EDLCs) store electrical energy through ion adsorption[8] and faradaic capacitors or pseudo-capacitors store electrical energy through fast redox reactions.[9,10] EDLCs work primarily with carbon-based materials characterized by

high surface area, mechanical resistance, and good electrical conductivity, which result in long life cycle and high power density.[11,12] However, their commercial application is questioned by the relatively low specific capacitance.[13,14] Metal oxides/hydroxides and conductive polymers are generally utilized for faradaic capacitor materials. Their ability to display various oxidation states with significant charge transfer reactions makes them capable of achieving high specific capacitance and energy density.[15] However, despite their potential benefits, these materials have low stability and poor electrical conductivity, which are not useful in practical applications.[16,17]

According to previous studies, ruthenium oxide (RuO_2) is amongst the earliest metal oxides to be studied as a traditional pseudocapacitive electrode material.[18] However, ruthenium in its elemental form is costly, hindering the achievement of commercial applications with high-efficiency rates.[19] Therefore, some inexpensive transition metal oxides, including NiO,[20] SnO_2,[21] MnO_2[22] and Co_3O_4,[23] were manufactured as alternative materials. Among these metal oxides, Co_3O_4, with a theoretical specific capacitance of 3560 F g^{-1}, is a fascinating electrode material for SCs.[24] Nevertheless, the cycling stability of Co_3O_4 is still a challenge for practical applications. The spinel cobaltite MCo_2O_4 (M = Ni, Cu, Mn) derived from Co_3O_4 is considered promising due to the mixed valence metal cations, which

provide better electrochemical performances compared to single-metal oxides.[25,26] Mesoporous Co_3O_4 nanocubes reported by Liu *et al.*[23] exhibit 220 F g^{-1} capacitance and good stability. Flower-like $MnCo_2O_4$ hollow microspheres[27] and pod-like $MnCo_2O_{4.5}$ microstructures[19] synthesized using a solvothermal method yield 235.7 and 321 F g^{-1} of capacitances and 93% (after 2000 cycles) and 87% (after 4000 cycles) capacitance retention, respectively. Porous hexagonal $NiCo_2O_4$ nanoplates synthesized by Pu *et al.*[28] exhibit a capacitance of 294 F g^{-1} and 89.8% capacity retention after 3000 cycles.

Studies have also reported that porous carbon combined with metal oxides increases the electrochemical activity and stability of the obtained composite. Recently, various carbon-based materials have been utilized to enhance the properties of metal oxides. The most used are reduced graphene oxide (rGO),[29–31] graphene,[32–34] activated carbon,[35–37] g-C_3N_4,[38,39] and carbon nanotubes (CNT).[40] They have excellent properties, such as large surface area and good conductivity, but their fabrication process from commercial precursors is however costly and environmentally harmful. Actually, biomass is a compelling choice for creating carbon-based materials due to its renewability, sustainability, environmental friendliness, and low cost.[41,42]

A variety of biomass, including orange peel,[43] watermelon,[44] peanut shell waste,[45] flower,[17] dead leaves,[46] rice husks,[47] and *Hibiscus sabdariffa*,[16] have been used to synthesize metal oxides/carbon composites for supercapacitor applications.[48–50] For example, Qian Li *et al.*[17] fabricated $Ni(OH)_2$ on carbon microtubes from willow catkins. The asymmetric device in 6 M KOH displayed energy and power densities of 37 W h kg^{-1} and 750 W kg^{-1}, respectively. Shan Liu *et al.*[51] produced lignin-derived porous carbon nanofibers (Co_3O_4–CNFs) *via* electrospinning and demonstrates a capacitance of 369 F g^{-1} at 0.1 A g^{-1}. Nan *et al.*[52] also obtained $NiCo_2O_4$ with carbon from poplar catkins. The as-prepared electrode exhibits a capacitance of 1538 F g^{-1} (922.9 C g^{-1}) at 1 A g^{-1}, which retains 91.4% of its value after 5000 cycles.

Additionally, biomass liquid extracts can also be employed, besides carbon sources, as green catalysts to synthesize metal oxide nanoparticles. Kundu *et al.*[53] used *Hydrangea paniculata* flower extracts to fabricate nickel oxide nanoparticles (NiO-NPs) for supercapacitor electrode materials. For the same purpose, B. D. Ngom *et al.*[16] also successfully synthesized vanadium pentoxide carbon composite (V_2O_5@C) derived from the natural *Hibiscus sabdariffa* (HS) family using a green solvothermal process. They concluded that a high amount of carbon from the HS extract was incorporated into the V_2O_5 matrix, which improved the electrochemical performances.

The synthesis procedures of these carbon-based materials are mostly time-consuming and energy-intensive, and therefore, are very expensive for large-scale applications. In this regard, the extract from plant waste can be used as a renewable carbon precursor and integrated into a nickel–cobalt matrix for low-cost and sustainable electrode material.

Therefore, *Anacardium occidentale* (AO), a cultivable plant belonging to the family of Anacardiaceae as natural and renewable biomass, has been used sparingly to fabricate carbon-based materials. This tropical plant can grow up to 15 m tall. It has a twisted and thick trunk with woody branches.[54] Several studies performed on leaf, stem, and bark extracts to isolate chemical compounds showed that the different parts contain many bioactive molecules, some of them being represented in Fig. S1.†[54–56]

In the present study, we prepared a composite nickel cobaltite hydroxide, $NiCo_2O_4$/NiOOH (NiCoO), with biomass carbon (BC) from the bark of *Anacardium occidentale* (AO) *via* a facile shot-step hydrothermal process at low temperature (150 °C) for different synthesis time durations of 2 h, 4 h, 8 h, 16 h. The dye extracted from AO containing bioactive molecules like phenolic acid functional groups was employed as a green catalyst for metal oxide fabrication[16,57] and carbon source. The filtered waste of the bark is further used to fabricate activated carbon and extract lignin and cellulose. In this regard, we will value all the parts of the bark to produce sustainable and renewable materials for supercapacitor electrodes. We also consider the importance of the survival of the plant and the large-scale application. During the collection, we do not remove the bark totally, so the plant does not suffer from any problems and develops new bark in a short period. Actually, the quantity used at a laboratory scale is not so important; however, the AO is a cultivable plant that can be easily developed for large-scale applications.

The BC incorporated into nickel–cobalt hydroxide was examined using XPS, Raman, and EDS mapping images.

The electrochemical performance of the NiCoO@BC composite analyzed firstly with a three-electrode system revealed better specific capacitance and stability than pristine NiCoO without biomass carbon. Moreover, the NiCoO@BC(4 h) composite as a positive electrode in an asymmetric supercapacitor NiCoO@BC(4 h)//AC with AC in the opposite electrode provides good energy/power density. This work offers fresh ideas for future advances in developing electrode materials for supercapacitors using energy-saving processes and promotes biomass use for energy storage.

2. Material synthesis

2.1. Materials

Reagents $Co(SO_4)\cdot 7H_2O$ (purity 99%), $Ni(NO_3)_2\cdot 6H_2O$, (purity 99%), and potassium hydroxide (KOH, min 85%) purchased from Sigma-Aldrich were directly used without any purification. The barks of *Anacardium occidentale* (AO) were collected in Senegal. A 3D scaffold nickel foam (thickness: 1.6 mm, areal density: 420 g m^{-2}) was used as material support and current collector.

2.2. Preparation of the NiCoO@BC composite

Two steps were used to synthesize NiCoO@BC composites from the barks of AO: dye extraction and hydrothermal synthesis. The barks were first air-dried naturally, crushed into a fine powder using a blender, and 3 g of the crushed barks were mixed into 150 mL of distilled water. The mixture, after stirring for 2 h, was left to stand for 24 h at ambient temperature to make sure that

bioactive compounds were fully extracted and then filtered to obtain the dye, as shown in Fig. 1a. Then, hydrothermal synthesis was performed using 1 g of $Co(SO_4) \cdot 7H_2O$, 0.5 g of $Ni(NO_3)_2 \cdot 6H_2O$, and 30 mL of the above dye obtained from AO. This mixture was dissolved under continuous magnetic stirring for up to 2 hours to homogenize the solution and then transferred into an electric oven at 150 °C for different synthesis time durations to obtain a brown color powder as shown in Fig. 1b and named nickel cobaltite oxide biomass carbon (NiCoO@BC). The same steps were used to fabricate either pristine NiCoO with no added dye as a sample reference or other NiCoO@BC samples at different synthesis time durations of 2 h, 4 h, 8 h, and 16 h.

2.3. Synthesis of activated carbon (AC)

A raw material, peanut shell waste (PSW), was used to fabricate AC through a conventional direct pyrolysis technique reported by Sylla *et al.*[45] Briefly, the PSW was collected, washed with deionized water, dried under direct sunlight for over 12 h, and crushed into fine powder. The mixture of 5 g of PSW powder, 1 g of NaCl, and 0.5 g of urea with deionized water (a few drops) was dried at 80 °C overnight and then transferred into a furnace under a 250 sccm argon flow for 2 h at 600 °C. The obtained black product was mixed with porosity-enhancing KOH agents and submitted to pyrolysis at 850 °C for 1 h under 250 sccm argon flow. After filtering, the solid material was washed with deionized water until neutral pH and then dried at 80 °C for 12 hours.

3. Characterization methods

Structural and morphological properties were examined by (i) X-ray diffraction measurements (Bruker D8 Advance, $\lambda = 1.542$ Å), (ii) Raman spectroscopy (laser wavelength $\lambda = 473.1$ nm), (iii) X-ray photoelectronic spectrometry (model: VG Escalab 220i XL, Al Kα 1,2 polychromatic source $h\nu = 1486.6$ eV), (iv) scanning electron microscopy (Tescan Vega3 LMH) and (v) transmission electron microscopy (model: JEM 2100 F, 200 kV). The porosity was evaluated by nitrogen adsorption–desorption measurements (relative pressure P/P_0: from 0.0 to 1.0) using the Brunauer–Emmett–Teller analysis (BET: Quantachrome), and the specific surface area was determined by BET theory. The electrochemical study was performed using a Biologic VMP 300 instrument, reference electrode (Ag/AgCl: 3 M KCl saturated), and platinum plate counter electrode.

4. Preparation of electrode material

To prepare the working electrode, conductive carbon black (10%), active material (80%), and polyvinylidene fluoride (10%) as a binder were mixed with a low-viscosity solvent NMP (N-methyl-2-pyrrolidone) to disperse the active material.[58] The obtained slurry was pasted on a current collector (nickel foam) and then dried for 12 h at 60 °C in an oven to obtain the electrode. The active material was coated on a surface of about 1 cm² for all the electrodes. Then, a similar process was employed to fabricate positive (NiCoO@BC(4 h)) and negative (AC) electrodes for
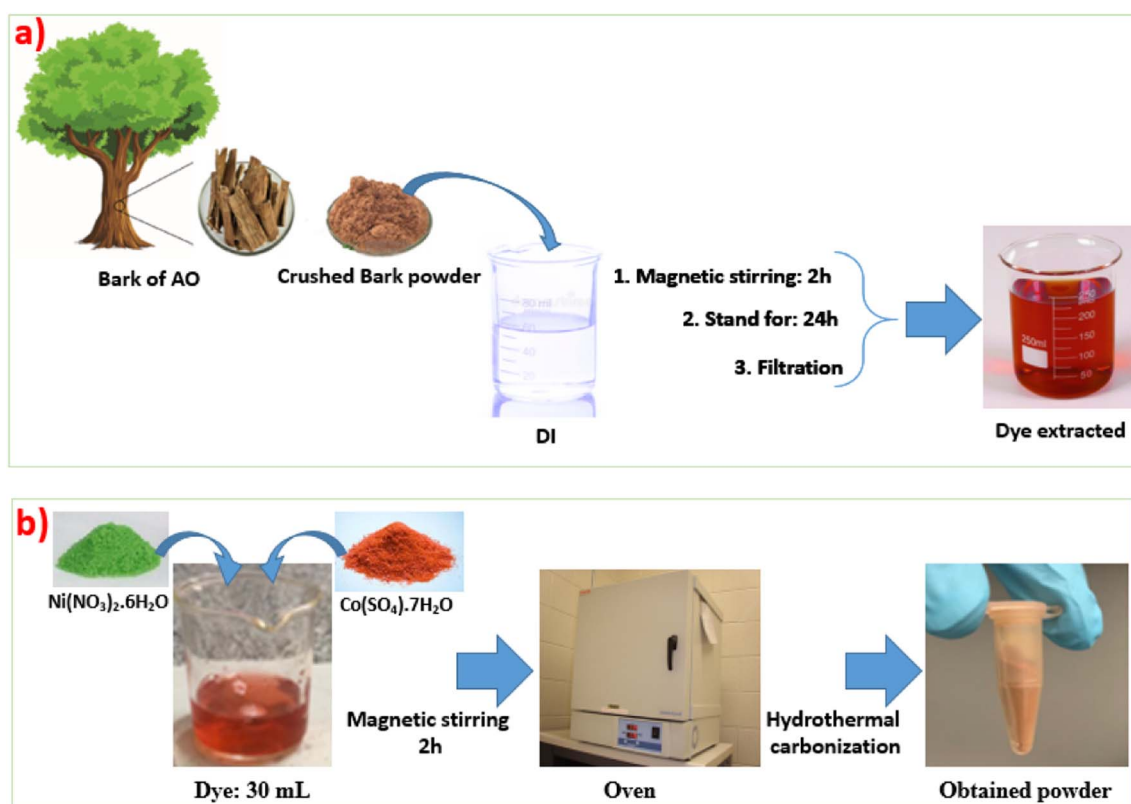

Fig. 1 (a) Schematic process for the extraction of dye from *Anacardium occidentale* (AO), (b) hydrothermal synthesis steps of NiCoO@BC.

© 2024 The Author(s). Published by the Royal Society of Chemistry

assembling a full device (Swagelok system; stainless steel plungers) using filter paper as electrode separator in 6 M KOH.

5. Results and discussion

5.1. Material characterizations

XRD spectra of the pristine and the composites prepared in 2 h, 4 h, 8 h, and 16 h synthesis time durations, as shown in Fig. 2a and S2a,† are in agreement with the hexagonal structure of NiOOH and the spinel $NiCo_2O_4$ peak patterns. The prominent peaks at 18.4°, 36.5°, 44.0°, 55.0°, and 59.0° were ascribed respectively to (111), (311), (400), (422), and (511) planes of spinel $NiCo_2O_4$ which belong to the $Fd\bar{3}m$ space group system, a cubic crystal structure with face-centered identified through JCPDS file (no. 20-0781).[59,60] $NiCo_2O_4$ has a spinel structure with Co^{2+} cations located in tetrahedral sites, while Ni^{3+} and Co^{3+} cations are situated in octahedral sites.[59] NiOOH exhibits three peaks at 12.0°, 25.2°, and 41.0°, which are consistent with the (003), (006), and (104) planes of the hexagonal structure according to Database (ICSD) Card No. 06-0075.[61–63]

The diffraction peaks of the obtained carbon are not observed because of the amorphous nature of the biomass carbon. Nevertheless, the presence of carbon is confirmed through Raman spectra, as shown in Fig. 2b, which shows three bands: G, D, and 2D. The D and G bands are observed at 1320 and 1560 cm^{-1}, respectively, in two broad overlapping peaks.[14] The G band correlated with the in-plane stretching sp^2 carbon vibration in graphite-like structure is beneficial for charge storage.[64] As for the D band, it refers to disordered sp^2 carbon, which is valuable for electrical conductivity.[64] Furthermore, in the range 2600–3000 cm^{-1}, a broad band appears as the Raman signature of the carbon 2D-band (an overtone of the D band), confirming the presence of amorphous carbon in the composites.[65] Fig. S2b† compares the Raman spectra of pristine NiCoO without biomass carbon and the NiCoO@BC(4 h) composite. As displayed, the presence of carbon peaks in the composite confirms the incorporation of carbon from the bark of AO extract into the nickel–

cobalt hydroxide matrix. The intensity ratio (I_D/I_G) for the sample NiCoO@BC(4 h) was calculated to be 0.82, implying that numerous defects exist in the carbon amorphous structure. According to Nan *et al.*,[52] multiple structural defects can lead to improved conductivity by creating more attachment sites for metal ions. Previous studies[66,67] have demonstrated A_{1g}, E_g, and three F_{2g} bands as the five Raman active modes in the ideal spinel structure. The octahedral and the tetrahedral cation vibration modes F_{2g}, E_g, and A_{1g} (for CoO and NiO) are observed at 245, 486, and 630 cm^{-1}, respectively.[28] The other band at 3400 cm^{-1} in the pristine material refers to the OH vibration mode from NiOOH.[68]

The XPS measurement was performed to identify the elemental composition of the NiCoO@BC composite and to confirm the presence of carbon. The survey spectra shown in Fig. S3a† exhibit the peaks of O, C, Co, and Ni elements. These results are consistent with those obtained through XRD and Raman patterns. Therefore, in order to investigate the carbon amount in the different samples, the atomic percentage is calculated from XPS spectra and represented *versus* the synthesis time durations in Fig. 3a. The NiCoO@BC(4 h) sample heat-treated at 4 h contains higher carbon (45%) and lower oxygen concentrations than the other samples.

The percentage of carbon increases from 2 h to 4 h synthesis duration and decreases beyond this time limit. This result reveals that a 4 h synthesis duration at 150 °C is the optimized reaction condition required to maximize the amount of carbon. The decrease in the amount of carbon is due to the formation of CO_2, which is released in gaseous form after the optimum synthesis time duration.

Fig. 3b–e displays the XPS deconvolution of C 1s, O 1s, Ni 2p, and Co 2p for the NiCoO@BC(4 h) composite. The core-level spectra of C 1s and O 1s peaks show the binding energies C–O, C–C, and C=O in the carbon matrix and O-metal bonds (Fig. 3b and c).

The high-resolution spectrum of Ni 2p is fitted into two peaks at 856 eV and 858 eV corresponding to the Ni^{2+} and Ni^{3+} oxidation states, respectively, and a less intense satellite peak
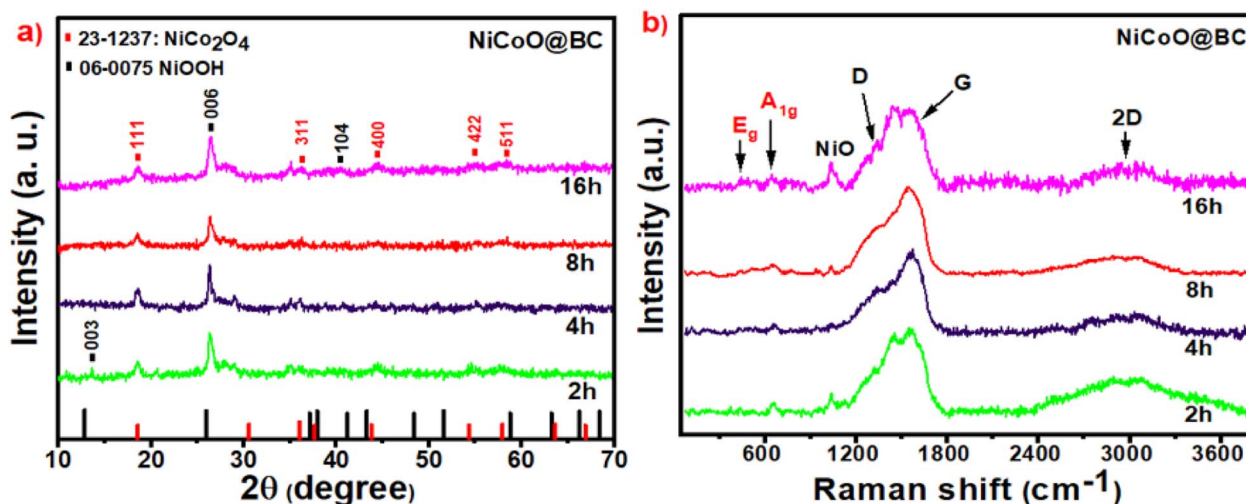

Fig. 2 (a) XRD peak patterns and (b) Raman spectra of NiCoO@BC composites at different synthesis time durations of 2 h, 4 h, 8 h, and 16 h.
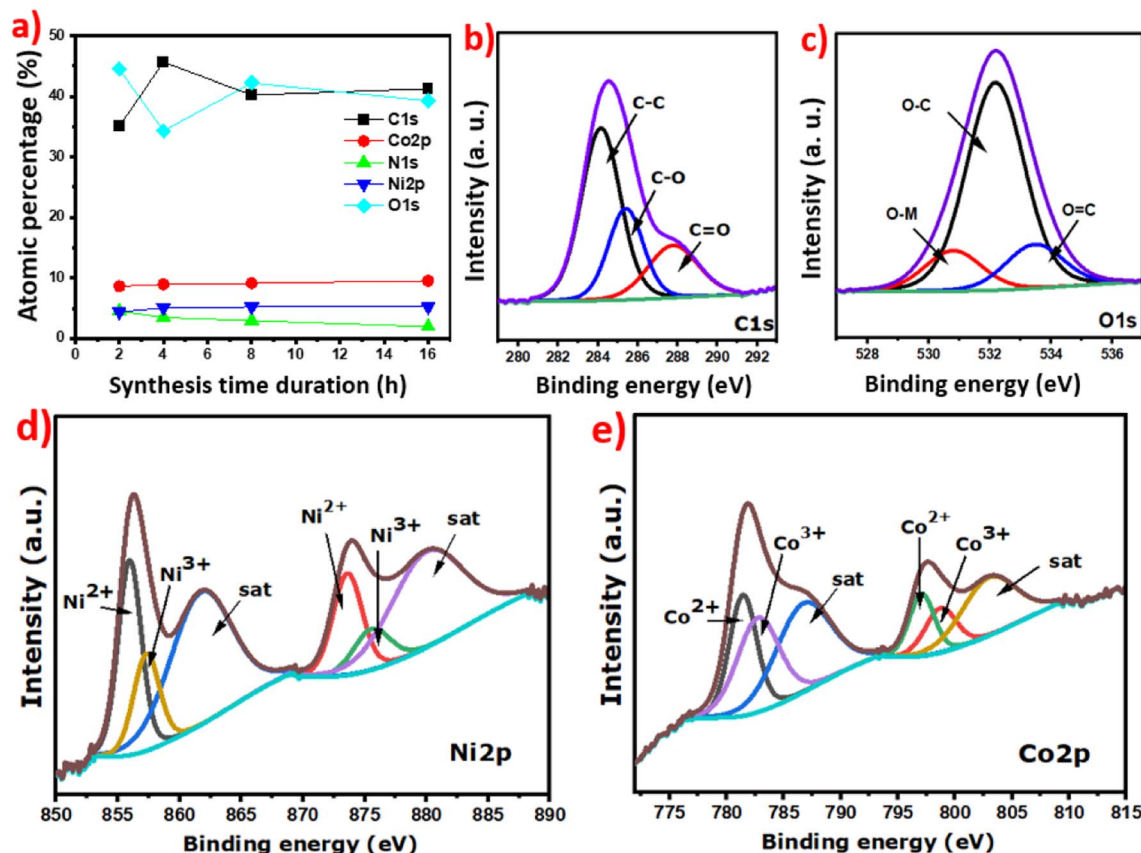
Fig. 3 (a) Atomic percentage *versus* synthesis time duration (2 h, 4 h, 8 h, 16 h) and (b)–(e) fitted spectra of C, O, Co, and Ni elements of NiCoO@BC(4 h).

appears at 862 eV (Fig. 3d).[34] The Co 2p spectrum fitted in a similar way shows two oxidation states, Co^{2+} at 781 eV and Co^{3+} at 783 eV, and a satellite peak at 787 eV (Fig. 3e). These outcomes mean that Co^{3+}/Co^{2+} and Ni^{3+}/Ni^{2+} redox couples coexist in the metal oxide structure of the NiCoO@BC composites. These redox couples create multiple electroactive sites, enhancing the electrochemical performance.[38,52] Small amount of nitrogen noticed in the composites is originated from the bark of AO, which has 2.1% nitrogen content (Fig. S3b†). That percentage of nitrogen and carbon in the bark of AO is more than those in other biomass parts reported by Raimie H. H. Ibrahim *et al.*,[69] as shown in Table S1.† These nitrogen atoms can supply electron donors, which improve the wettability and the electrical conductivity of the NiCoO@BC composite as electrode material.[70] Additionally, the nitrogen introduced into the carbon matrix has the potential to generate significant pseudocapacitance through faradaic redox reactions in aqueous electrolytes.[14,71] The high-resolution spectra of all the elements in the composites for different synthesis time durations are presented in Fig. S4.† As observed, the nitrogen peak decreases significantly when the synthesis time duration is increased and almost disappears at 16 h, corresponding to the appearance of metal–carbon binding (M–C).

The morphological features from SEM images (low and high magnifications) of the NiCoO@BC(4 h) composite display

microsheet-like structures, as shown in Fig. 4a and b. The micrographs exhibit nanograins (20–50 nm) grown on random sheets. Energy dispersive X-ray spectroscopy (EDS) is used to obtain further information about the distribution of chemical elements within the composite. The mapping images represented in Fig. S5† show that carbon, cobalt, nickel, nitrogen, and oxygen elements are homogeneously distributed in the NiCoO@BC(4 h) composite.

For further morphological analysis, transmission electron microscopy (TEM) was performed. Nanograins and a transparent zone referring to the carbon material (Fig. 4c and d)[72] are clearly observed. The enlarged high-resolution images in Fig. 4e and f exhibit the presence of defined fringes in the composite structure. The distances between fringes (0.20, 0.24, and 0.46 nm) correspond to the (400), (311), and (111) planes of $NiCo_2O_4$ while those at 0.31 nm and 0.60 nm are associated with the (006) and (003) planes of the NiOOH hexagonal structure, in agreement with the XRD results.[73,74] Well-defined diffraction rings are also displayed by SAED (selected area electron diffraction) inserted in Fig. 4e, indicating that the nanomaterials possess a polycrystalline structure.[75]

The distribution of the NiCoO@BC(4 h) pore size was examined with N_2 adsorption/desorption analysis. Fig. 4g displays an isotherm type IV, with hysteresis loops of H4 according to the IUPAC classification.[17,45,76] NiCoO@BC(4 h) displays a specific
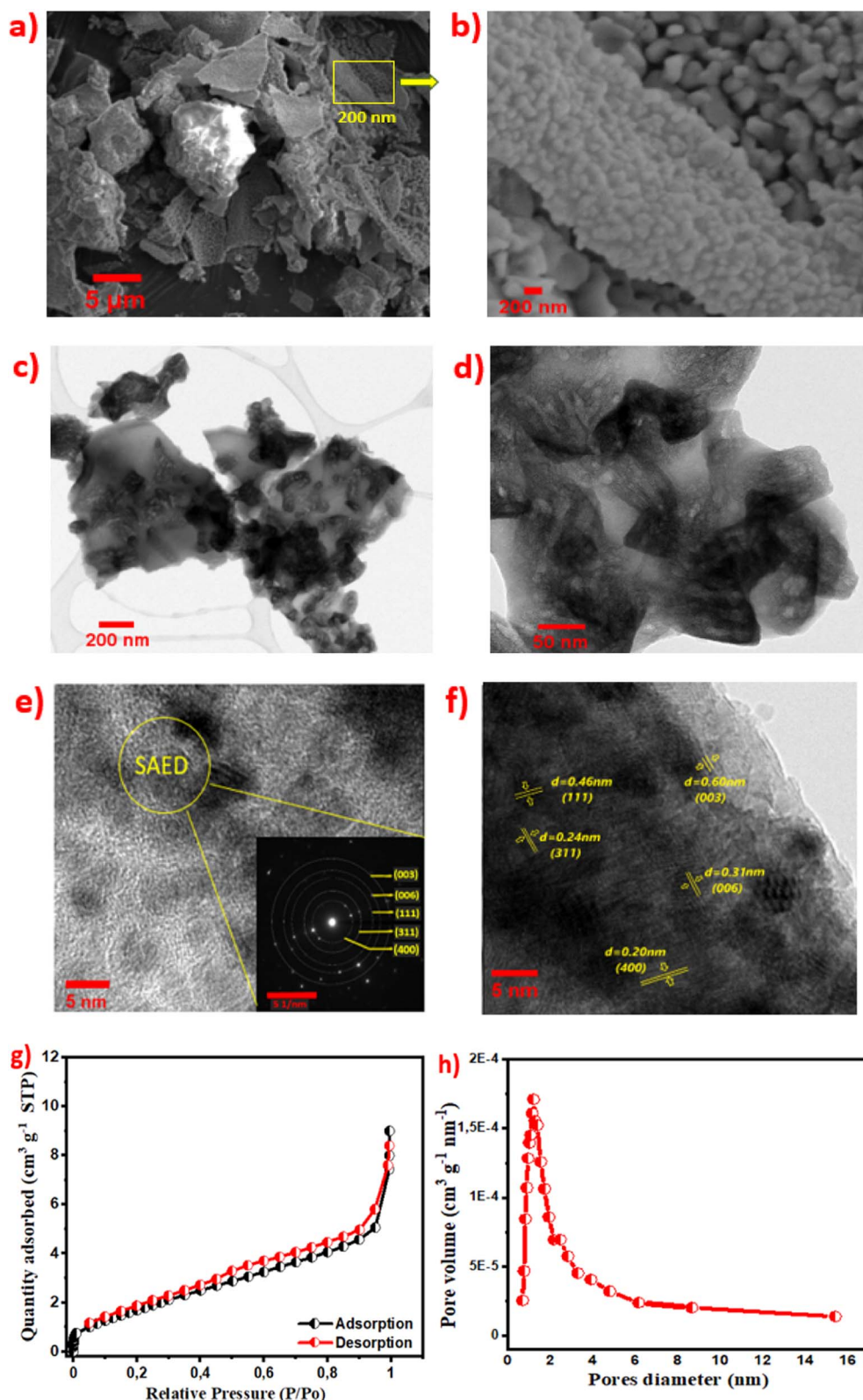
Fig. 4 (a and b) SEM and (c–f) TEM (with SAED) images, (g) absorption/desorption N$_2$ isotherm, (h) pore size distribution of the NiCoO@BC(4 h) composite.

surface area of 5.2 m^2 g^{-1} from BET analysis.[77,78] The corresponding pore size distribution shown in Fig. 4h indicates that most pores lie in the micro and mesopores range. This mesoporous structure enhances the diffusion of electrolyte ions, which improves charge transport and provides more electroactive sites. This feature is advantageous for energy storage.[28,60]

5.2. Electrochemical studies

Electrochemical measurements of NiCoO and NiCoO@BC composites were carried out by cyclic voltammetry (CV), galvanostatic charge/discharge (GCD), and electrochemical impedance spectroscopy (EIS) using aqueous potassium hydroxide KOH (6 M) electrolyte.

The choice of this electrolyte was guided by its excellent properties for electrochemical studies, as shown in Table 1. KOH stands out for its high ionic conductivity (73.5 cm^2 Ω mol^{-1} for K$^+$) and small hydration sphere radius compared to neutral and acidic electrolytes (LiCl, KNO$_3$, Na$_2$SO$_4$, and KCl).[79-82] KOH concentration was also optimised by Xueqin Lang *et al.*[83] using 1 M, 3 M, and 6 M KOH for La$_{0.85}$Sr$_{0.15}$MnO$_3$@NiCo$_2$O$_4$ composite. They concluded that 6 M KOH gave better electrochemical performances. At a current density of 32 A g^{-1}, the material provided an optimal capacitance of 1341 F g^{-1} (with capacitance retention of 52%) in 6 M KOH electrolyte compared to 760 F g^{-1} (38% of capacitance retention) in 3 M and 400 F g^{-1} (10% of capacitance retention) in 1 M KOH.[82]

The working potential of all the samples was first optimized to be 0.5 V using the reference electrode (Ag/AgCl). Fig. 5a compares CV plots of the composites at different synthesis time durations (2 h, 4 h, 8 h, 16 h). The CV of the materials performed at a rate of 5 mV s^{-1} exhibits high current responses and faradaic behavior with cathodic oxidation and anodic reduction peaks.[61] The large curve areas also imply a capacitance contribution of the carbon-based material combined with reversible redox reactions of the metal oxides involving redox couples Co^{3+}/Co^{2+} and Ni^{3+}/Ni^{2+} into the composites, as suggested by XPS results. Previous studies have described the redox reaction mechanism using the following eqn (1) and (2).[19,84]

$$NiCo_2O_4 + H_2O + OH^- \leftrightarrow NiOOH + 2CoOOH + e^- \quad (1)$$

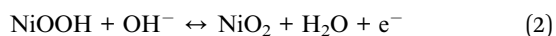$$NiOOH + OH^- \leftrightarrow NiO_2 + H_2O + e^- \quad (2)$$

Fig. 5b presents the GCD of all the samples recorded at 0.5 A g^{-1} over the same potential window of 0.5 V. The nonlinear curves confirm the faradaic behavior of the composites. GCD curves also display symmetric shapes, indicating the reversibility of the redox reactions during charging–discharging. Fig. 5c presents the specific capacitances *versus* current densities calculated from GCD using eqn (3):

$$C\left(\text{F g}^{-1}\right) = \frac{I\Delta t}{m\Delta V} \quad (3)$$

I (A) is the galvanometric current, C (F g^{-1}) is the specific capacitance, ΔV (V) is the working potential, Δt (s) is the discharge time, and m (g) is the mass of the active material on the electrode.

The electrode mass loading of the samples for 2 h, 4 h, 8 h, and 16 h synthesis time durations are determined to be around 2.7 mg ($\sim$2.7 mg cm^{-2}), and the specific capacitances at 0.5 A g^{-1} are calculated to be 468, 475, 442, and 328 F g^{-1}, respectively. In addition, 43%, 56%, 53%, and 66% of their value are retained from 0.5 to 10 A g^{-1} of current density.

Electrochemical impedance spectroscopy was further performed to provide a more comprehensive understanding of the material properties. EIS plots of the composites in Fig. 5d display a steep slope at low frequencies, revealing the existence of Warburg impedance (W) from electrolyte species diffusion into the electrode material.[61,85] The inserted Nyquist plots show that all the composite electrodes possess low resistance. The analyzed curves exhibit ESRs of 0.42, 0.36, 0.62, and 0.56 ohm for the samples at 2 h, 4 h, 8 h and 16 h, respectively. These low ESR values prove the importance of the biomass carbon-based material in the composites. In particular, it can be noted that the NiCoO@BC(4 h) sample with more carbon content (as shown in Fig. 3a) exhibits lower ESR and better current response, specific capacitance, and capacitance retention than samples with other time durations (2 h, 8 h, 16 h).

Fig. S6† compares the electrochemical performances of the NiCoO@BC(4 h) composite with those of pristine NiCoO. As shown in Fig. S6a,† the composite displays a superior current response compared to the pristine sample. The specific capacitances of the pristine sample and NiCoO@BC(4 h) composite from GCD (Fig. S6b†) are presented as a function of the current density in Fig. S6c.† The NiCoO@BC(4 h) composite retains more than 56% of its capacitance from 0.5 to 10 A g^{-1}, while the pristine sample suffers from a sharp capacitance drop, losing almost 80% of its capacitance value even at 2 A g^{-1}. The NiCoO@BC(4 h) composite also displays a lower ESR (0.36 ohm) than the pristine sample (1.00 ohm) (Fig. S6d†), which is efficient to enhance the charge transfer and improve the capacitance.[68] The good capacitance, conductivity, and rate capability can be assigned to the effective incorporation of nitrogen and carbon from biomass into the metal oxide matrix.

The CV curves of NiCoO@BC(4 h) obtained at various scans from 5 mV s^{-1} to 100 mV s^{-1} (see in Fig. 6a) show the existence of redox peaks. These oxidation and reduction peaks located at around 0.41 V and 0.28 V barely shift as the scan rate increases. However, their shape remains similar, suggesting that the electrode performs well at high scan rates. The GCD profiles between 0.5 A g^{-1} and 10 A g^{-1} are nonlinear, which confirms the faradaic behavior of the composite.[86]

Table 2 compares the results of the present work with some results reported in the literature. The obtained composites synthesized with the facile energy-saving process using biomass carbon display a good specific capacitance as compared to these other works. The stability was also tested by continuous GCD at 10 A g^{-1} up to 7000 cycles, and the corresponding stability curves are represented in Fig. 6c. It is observed that the NiCoO@BC(4 h) sample shows 98% of coulombic efficiency and maintains 72% of
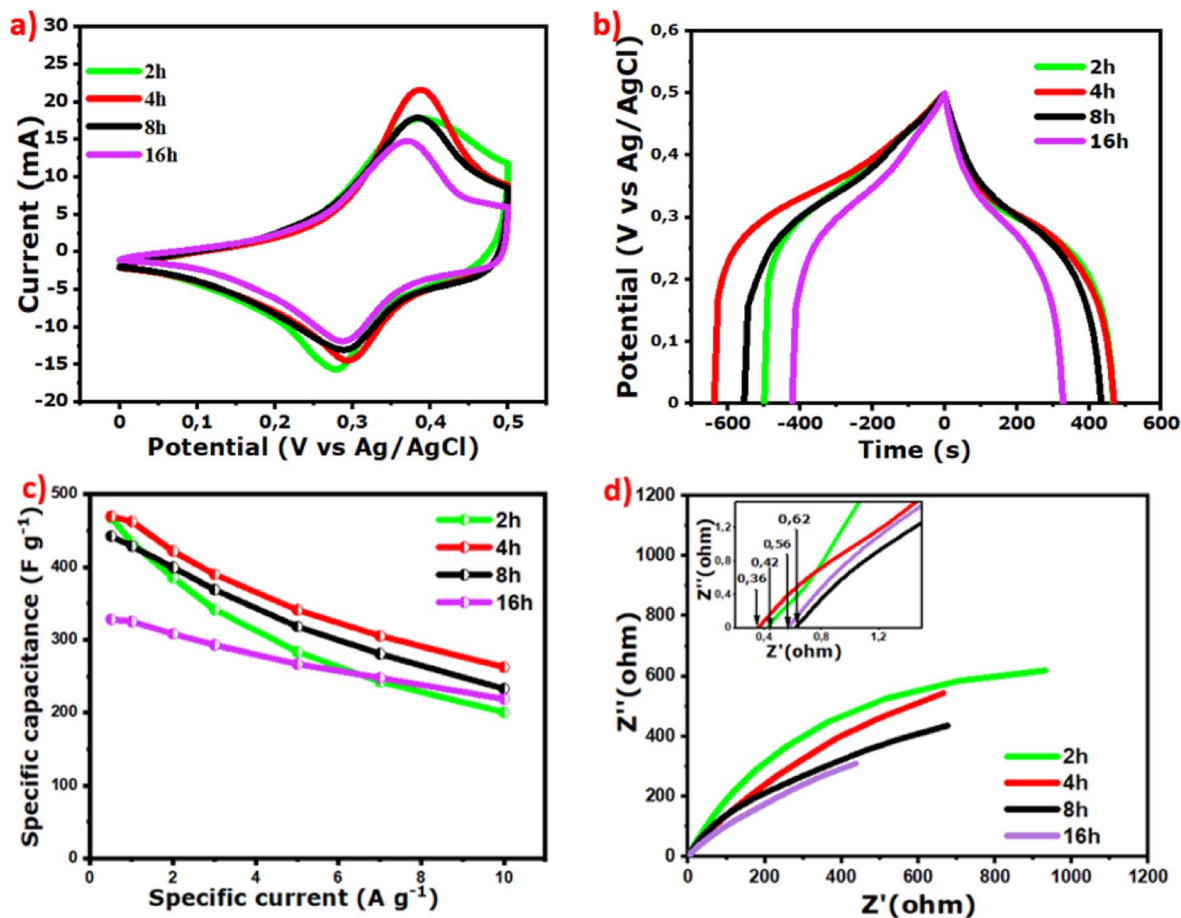
Table 1 Radius of the hydration sphere, molar conductivity, and ionic mobility of different ions

Item	Ion			
	OH$^-$	Cl$^-$	NO$_3^-$	SO$_4^{2-}$
Radius of hydration sphere (Å)	3.00	3.32	3.35	3.79
Molar conductivity (cm^2 Ω mol^{-1})	198.00	76.34	71.44	79.80
Ionic mobility ($\mu \times 10^{-5}$ cm^2 s^{-1} V^{-1})	20.60	7.91	4.40	8.30

Fig. 5 (a) CV plots at 5 mV s^{-1}, (b) GCD plots at 0.5 A g^{-1}, (c) C_s *versus* current density, and (d) EIS of NiCoO@BC samples for 2 h, 4 h, 8 h, and 16 h synthesis time durations.

its initial capacitance even after 7000 cycles, which indicates a good cycle life. The first 10 cycles, compared to the last 10 cycles of charging–discharging inserted in Fig. 6c, show no difference in cycle shape at a stable voltage of 0.5 V, confirming the excellent material stability. EIS, CV, and GCD measurements were performed after 7000 cycles and compared with the initial measurements. The ESR shown in Fig. 6d remains similar (0.38 Ω *vs.* 0.36 Ω) with a slow increase of diffusion resistance exhibited by the slight curve shift towards the *X* axis at low frequency. The CV curves show that the faradaic behavior of the composite is maintained with a slight decrease of the redox peaks, as shown in Fig. 6e. The GCD profile in Fig. 6f displays practically the same shape after 7000 cycles, indicating that the electrode performances are almost conserved.

To further examine the practicality of the NiCoO@BC composite, an ASC (NiCoO@BC(4 h)//AC) was assembled, with AC as the negative electrode and NiCoO@BC(4 h) composite as the positive electrode. The electrochemical performances of AC were tested in a three-electrode system, as shown in Fig. S7.† At 5 mV s^{-1}, the CV plots in the potential window from −1 to 0.2 V exhibit an ideal capacitive behavior indicated by rectangular-like profiles (Fig. S7a†).[88] The linear GCD curves at different current density values from 1 to 10 A g^{-1} correspond to a double-layer capacitive charge storage (Fig. S7b†).[13] AC

exhibits a specific capacitance of 160 F g^{-1} at 0.5 A g^{-1} and retains it well at a high current density of 10 A g^{-1} (Fig. S7c†) while the specific capacitance increases by 18% after 7000 cycles (Fig. S7d†).

The assembled full device using a Swagelok system (stainless steel plungers) and filter paper as the separator is schematically represented in Fig. 7a, and the CV of both composite and AC are displayed in Fig. 7b. The mass ratio of NiCoO@BC(4 h) (3.6 mg) and AC (4.4 mg) was calculated to be 0.8 based on the charge balance using eqn (4).

$$\frac{m_+}{m_-} = \frac{C_- \times \Delta V_-}{C_+ \times \Delta V_+} \tag{4}$$

m (g) is the mass of electrode materials, C (F g^{-1}) is the specific capacitance, and ΔV (V) is the potential window.

Fig. 7c exhibits the CV curves obtained with scan rates varying from 5 to 100 mV s^{-1} at a stable voltage of 1.6 V. The curves present a good current response and a large area indicating both faradaic and EDLC contributions corresponding to a hybrid-type supercapacitor. The nonlinear GCD plots in Fig. 7d at different current densities illustrate the faradaic contribution by the composite material, confirming the hybrid behavior of the device.
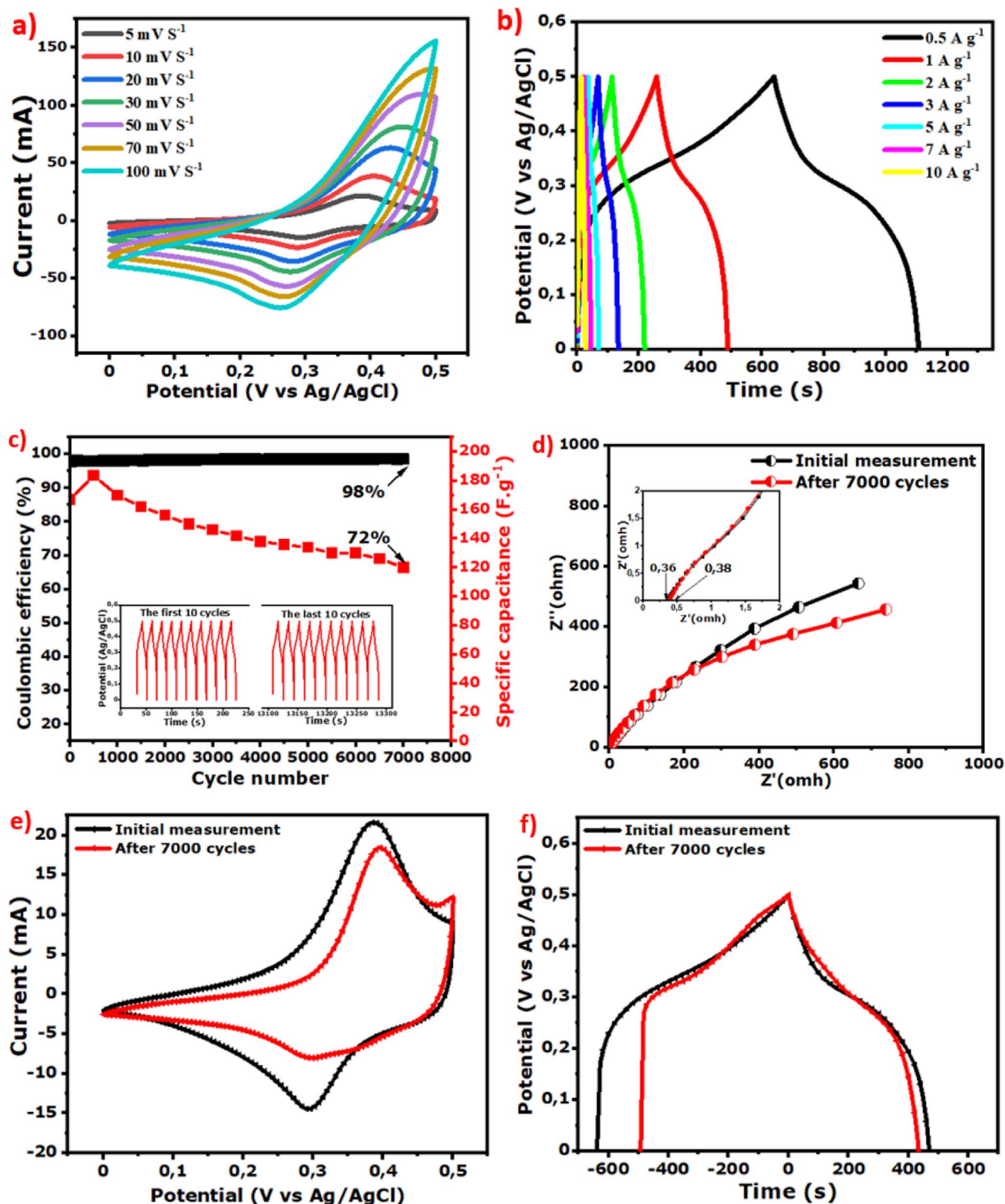
Fig. 6 (a) CV curves from 5 mV s^{-1} to 100 mV s^{-1}, (b) GCD profiles from 0.5 A g^{-1} to 10 A g^{-1}, (c) capacitance retention and coulombic efficiency after 7000 cycles at 10 A g^{-1} (d) EIS, (e) CV curves at 5 mV s^{-1} and (f) GCD profiles at 0.5 A g^{-1} after 7000 cycles compared to the initial measurements of the NiCoO@BC(4 h) composite.

The specific capacitance of the ASC calculated at 1 A g^{-1} from GCD is 50.2 F g^{-1}. When plotted *versus* current density, 65% of this value remains even at 10 A g^{-1}, which corresponds to a good rate capability (Fig. 8a). From GCD, the energy density (E_d) values and the corresponding power density (P_d) are also calculated using eqn (5) and (6) and plotted in a Ragone plot (Fig. 8b).

Table 2 Summary of electrochemical performances in comparison with some reported works

Electrodes	KOH electrolytes	Specific capacitances	Capacitance retention	Cycle number	References
$MnCo_2O_{4.5}$	2 M	321.0 F g^{-1}	87.0%	4000	19
$NiCo_2O_4$	1 M	294.0 F g^{-1}	89.8%	3000	28
$MnCo_2O_4$/carbon	3 M	235.6 F g^{-1}	86.0%	5000	87
$NiCo_2O_4@g-C_3N_4(C)$	6 M	325.7 F g^{-1}	93.6%	2000	39
Pristine NiCoO	6 M	353.0 F g^{-1}	51.0%	4000	This work
NiCoO@BC(4 h)	6 M	475.0 F g^{-1}	86.0%	4000	This work
			72.0%	7000	

$$E_d \left(W \ h \ kg^{-1}\right) = \frac{I_d}{3.6} \int V(t) dt \qquad (5)$$

$$P_d \left(W \ kg^{-1}\right) = 3600 \frac{E_s}{t} \qquad (6)$$

V (V) is the potential window, t (s) is the discharge time, and I_d (A g^{-1}) is the current density.

The E_d and P_d of the ASC calculated at 1 A g^{-1} are 20 W h kg^{-1} and 900 W kg^{-1}, respectively, and are superior or at least comparable to values reported in the literature, as shown in Fig. 8b.[14,19,77,89,90]

The EIS results of the device in Fig. 8c exhibit a low ESR of 0.17 Ω due to the synergy between the EDLC properties of AC for the negative electrode and the NiCoO@BC composite as a faradaic material for the positive electrode. The life cycle of the ASC, a crucial parameter for practical application, was evaluated at 10 A g^{-1} with 15 000 cycles (Fig. 8d). During the first 900 cycles, an increase in capacitance is observed. This could be because the electrode is gradually activated by the diffusion of electrolyte species within the material. The capacitance decreases slightly in the subsequent cycles because the whole device is fully activated and reaches its maximum wettability at 900 cycles, as
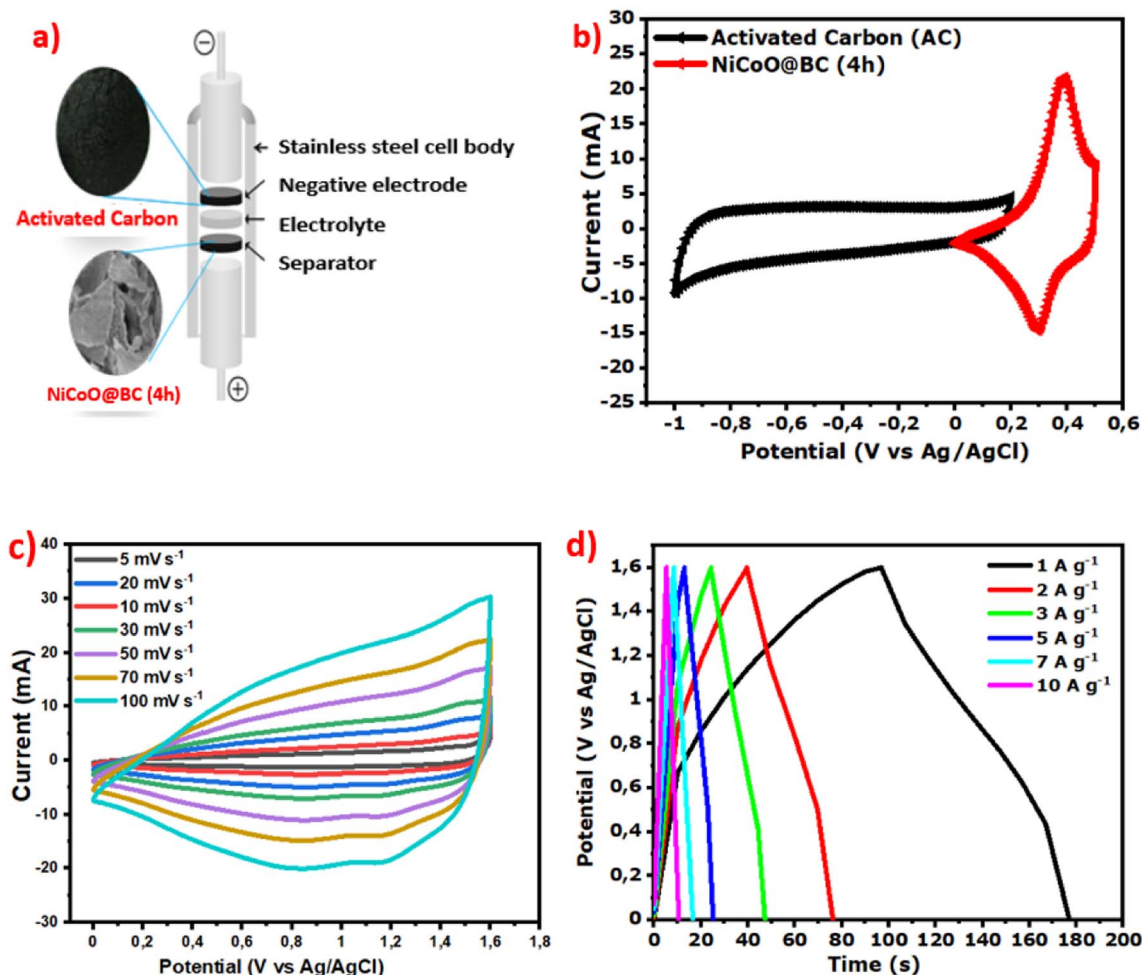

Fig. 7 (a) Assembled full device, (b) CV plots of NiCoO@BC(4 h) and AC, (c) CV plots from 5 to 100 mV s^{-1}, and (d) GCD profiles from 1 to 10 A g^{-1} of the device.
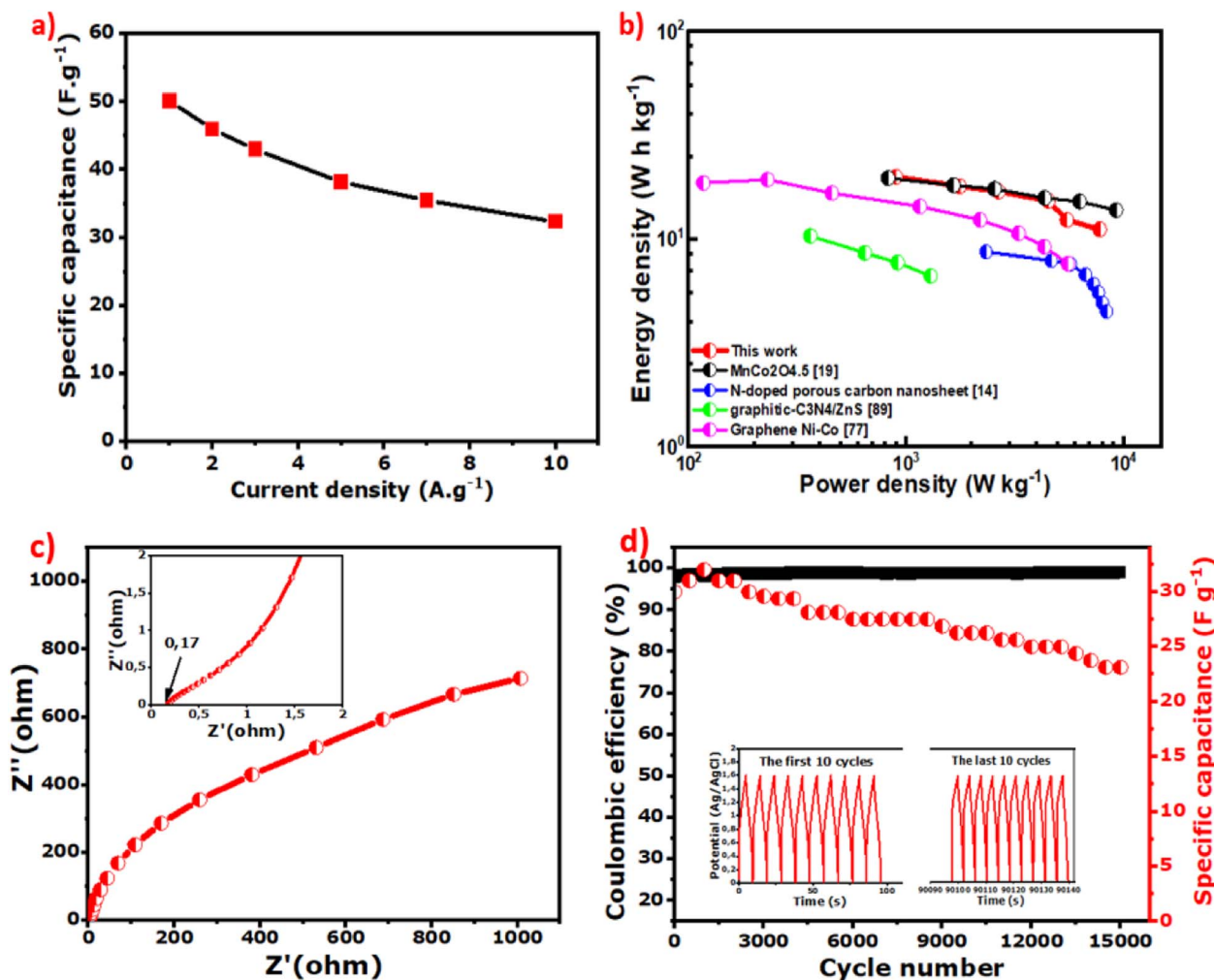
Fig. 8 (a) Specific capacitance *versus* current density, (b) Ragone plot of E_d as a function of P_d, (c) EIS curves (the inset is the ESR), and (d) capacitance retention and coulombic efficiency of the ASC device (NiCoO@BC(4 h)//AC) for up to 15 000 cycles.

explained by Q. Li *et al.*[17] The NiCoO@BC(4 h)//AC device shows an excellent coulombic efficiency of 99%, capacitance retention of 78% even after 15 000 cycles at 10 A g^{-1}, and no difference in cycle shape from the first to the last 10 charge–discharge cycles at a potential of 1.6 V, as shown in the inset of Fig. 8d.

6.   Conclusion

A green hydrothermal process was successfully developed to combine biomass carbon from the bark of AO with nickel cobaltite hydroxide NiCo$_2$O$_4$/NiOOH (NiCoO@BC) at low temperatures for different synthesis time durations. The highest amount of carbon was observed with the sample synthesized in 4 h. The synergy between metal oxide nanoparticles and biomass carbon allows good electrochemical performances. The NiCoO@BC(4 h) composite displays a low ESR of 0.36 Ω, good specific capacitance of 475 F g^{-1} at 0.5 A g^{-1}, as well as good stability. NiCoO@BC(4 h) was tested as a positive electrode in a full device with AC as a negative electrode. The system exhibits promising electrochemical performances for practical applications: a large potential window of 1.6 V, an energy density of 20 W h kg^{-1}, and a power density of 900 W kg^{-1}. The device also revealed good stability by retaining 99% coulombic efficiency, 65% of its specific capacitance from 0.5 A g^{-1} to 10 A g^{-1}, and a capacitance retention of 78% even after 15 000 cycles. Therefore, these promising results of the composite of nickel–cobalt oxide (NiCoO) and biocarbon derived from the bark of AO for supercapacitor electrodes make this technology suitable for clean energy for several applications, such as electronics, hybrid electric vehicles, *etc.*

Conflicts of interest

The authors declare that they have no known competing financial interests or personal relationships that could have appeared to influence the work reported in this paper.

Acknowledgements

References

1 M. S. Whittingham, History, evolution, and future status of energy storage, *Proc. IEEE*, 2012, **100**(Spl content), 1518–1534, DOI: **10.1109/JPROC.2012.2190170**.

2 X. Ge, *Materials for Energy Infrastructure*, 2016, pp. 83–91, DOI: **10.1007/978-981-287-724-6**.

3 Y. Qu, *et al.*, Tuning the crystal structure of NiS/carbon by Mo doping for asymmetric supercapacitor application, *Mater. Today Chem.*, 2022, **26**, DOI: **10.1016/j.mtchem.2022.101188**.

4 L. Kouchachvili, W. Yaïci and E. Entchev, Hybrid battery/supercapacitor energy storage system for the electric vehicles, *J. Power Sources*, 2018, **374**(November 2017), 237–248, DOI: **10.1016/j.jpowsour.2017.11.040**.

5 S. Faraji and F. N. Ani, Microwave-assisted synthesis of metal oxide/hydroxide composite electrodes for high power supercapacitors - a review, *J. Power Sources*, 2014, **263**, 338–360, DOI: **10.1016/j.jpowsour.2014.03.144**.

6 K. Zhang, L. L. Zhang, X. S. Zhao and J. Wu, Graphene/polyaniline nanofiber composites as supercapacitor electrodes, *Chem. Mater.*, 2010, **22**(4), 1392–1401, DOI: **10.1021/cm902876u**.

7 C. Arbizzani, *et al.*, Good practice guide for papers on supercapacitors and related hybrid capacitors for the Journal of Power Sources, *J. Power Sources*, 2020, **450**, 227636, DOI: **10.1016/j.jpowsour.2019.227636**.

8 F. Ma, S. Ding, H. Ren and Y. Liu, Sakura-based activated carbon preparation and its performance in supercapacitor applications, *RSC Adv.*, 2019, **9**(5), 2474–2483, DOI: **10.1039/c8ra09685f**.

9 S. Zhou, S. Cui, W. Wei, W. Chen and L. Mi, Development of high-utilization honeycomb-like α-Ni(OH)$_2$ for asymmetric supercapacitors with excellent capacitance, *RSC Adv.*, 2018, **8**(65), 37129–37135, DOI: **10.1039/c8ra08019d**.

10 A. K. Yedluri and H. J. Kim, Enhanced electrochemical performance of nanoplate nickel cobaltite (NiCo$_2$O$_4$) supercapacitor applications, *RSC Adv.*, 2019, **9**(2), 1115–1122, DOI: **10.1039/c8ra09081e**.

11 M. M. Sk, P. Pradhan, B. K. Patra and A. K. Guria, Green biomass derived porous carbon materials for electrical double-layer capacitors (EDLCs), *Mater. Today Chem.*, 2023, **30**, DOI: **10.1016/j.mtchem.2023.101582**.

12 A. Velasco, *et al.*, Recent trends in graphene supercapacitors: from large area to microsupercapacitors, *Sustain. Energy Fuels*, 2021, **5**(5), 1235–1254, DOI: **10.1039/d0se01849j**.

13 N. F. Sylla, *et al.*, Ex situ nitrogen-doped porous carbons as electrode materials for high performance supercapacitor, *J. Colloid Interface Sci.*, 2020, **569**, 332–345, DOI: **10.1016/j.jcis.2020.02.061**.

14 D. Wang, *et al.*, Coal tar pitch derived N-doped porous carbon nanosheets by the in situ formed g-C$_3$N$_4$ as a template for supercapacitor electrodes, *Electrochim. Acta*, 2018, **283**, 132–140, DOI: **10.1016/j.electacta.2018.06.151**.

15 N. Zhao, *et al.*, Entire synergistic contribution of electrodeposited battery-type NiCo$_2$O$_4$@Ni$_{4.5}$Co$_{4.5}$S$_8$ composite for high-performance supercapacitors, *J. Power Sources*, 2019, **439**(June), 227097, DOI: **10.1016/j.jpowsour.2019.227097**.

16 B. D. Ngom, N. M. Ndiaye, N. F. Sylla, B. K. Mutuma and N. Manyala, Sustainable development of vanadium pentoxide carbon composites derived from: Hibiscus sabdariffa family for application in supercapacitors, *Sustain. Energy Fuels*, 2020, **4**(9), 4814–4830, DOI: **10.1039/d0se00779j**.

17 Q. Li, *et al.*, β-Ni(OH)$_2$ Nanosheet Arrays Grown on Biomass-Derived Hollow Carbon Microtubes for High-Performance Asymmetric Supercapacitors, *ChemElectroChem*, 2018, **5**(9), 1279–1287, DOI: **10.1002/celc.201800024**.

18 V. Subramanian, S. C. Hall, P. H. Smith and B. Rambabu, Mesoporous anhydrous RuO$_2$ as a supercapacitor electrode material, *Solid State Ionics*, 2004, **175**(1–4), 511–515, DOI: **10.1016/j.ssi.2004.01.070**.

19 H. Chen, X. Du, J. Sun, Y. Wang, Y. Zhang and C. Xu, Solvothermal synthesis of novel pod-like MnCo$_2$O$_{4.5}$ microstructures as high-performance electrode materials for supercapacitors, *Int. J. Hydrogen Energy*, 2020, **45**(4), 3016–3027, DOI: **10.1016/j.ijhydene.2019.11.153**.

20 Y. Q. Zhang, *et al.*, Self-assembled synthesis of hierarchically porous NiO film and its application for electrochemical capacitors, *J. Power Sources*, 2012, **199**, 413–417, DOI: **10.1016/j.jpowsour.2011.10.065**.

21 U. Nithiyanantham, A. Ramadoss and S. Kundu, Synthesis and characterization of DNA fenced, self-assembled SnO$_2$ nano-assemblies for supercapacitor applications, *Dalton Trans.*, 2016, **45**(8), 3506–3521, DOI: **10.1039/c5dt04920b**.

22 F. Liao, *et al.*, MnO$_2$ hierarchical microspheres assembled from porous nanoplates for high-performance supercapacitors, *Ceram. Int.*, 2019, **45**(1), 1058–1066, DOI: **10.1016/j.ceramint.2018.09.285**.

23 X. Liu, *et al.*, Facile and green synthesis of mesoporous Co$_3$O$_4$ nanocubes and their applications for supercapacitors, *Nanoscale*, 2013, **5**(14), 6525–6529, DOI: **10.1039/c3nr00495c**.

24 Z. Liu, *et al.*, Facile synthesis of homogeneous core-shell Co$_3$O$_4$ mesoporous nanospheres as high performance electrode materials for supercapacitor, *J. Alloys Compd.*, 2019, **774**, 137–144, DOI: **10.1016/j.jallcom.2018.09.347**.

25 A. Pendashteh, *et al.*, Highly Ordered Mesoporous CuCo$_2$O$_4$ Nanowires, a Promising Solution for High-Performance Supercapacitors, *Chem. Mater.*, 2015, **27**(11), 3919–3926, DOI: **10.1021/acs.chemmater.5b00706**.

26 C. W. Cady, *et al.*, Tuning the electrocatalytic water oxidation properties of AB$_2$O$_4$ spinel nanocrystals: A (Li, Mg, Zn) and B (Mn, Co) site variants of LiMn$_2$O$_4$, *ACS Catal.*, 2015, **5**(6), 3403–3410, DOI: **10.1021/acscatal.5b00265**.

27 H. Che, A. Liu, J. Mu, C. Wu and X. Zhang, Template-free synthesis of novel flower-like MnCo$_2$O$_4$ hollow microspheres for application in supercapacitors, *Ceram. Int.*, 2016, **42**(2), 2416–2424, DOI: **10.1016/j.ceramint.2015.10.041**.

28 J. Pu, J. Wang, X. Jin, F. Cui, E. Sheng and Z. Wang, Porous hexagonal NiCo$_2$O$_4$ nanoplates as electrode materials for

supercapacitors, *Electrochim. Acta*, 2013, **106**, 226–234, DOI: **10.1016/j.electacta.2013.05.092**.

29 P. Siwatch, K. Sharma, N. Singh, N. Manyani and S. K. Tripathi, Enhanced supercapacitive performance of reduced graphene oxide by incorporating $NiCo_2O_4$ quantum dots using aqueous electrolyte, *Electrochim. Acta*, 2021, **381**, 138235, DOI: **10.1016/j.electacta.2021.138235**.

30 Z. Wei, J. Guo, M. Qu, Z. Guo and H. Zhang, Honeycombed-like nanosheet array composite $NiCo_2O_4$/rGO for efficient methanol electrooxidation and supercapacitors, *Electrochim. Acta*, 2020, **362**, DOI: **10.1016/j.electacta.2020.137145**.

31 H. Jiang, K. Yang, P. Ye, Q. Huang, L. Wang and S. Li, Optimized $NiCo_2O_4$/rGO hybrid nanostructures on carbon fiber as an electrode for asymmetric supercapacitors, *RSC Adv.*, 2018, **8**(65), 37550–37556, DOI: **10.1039/c8ra07477a**.

32 H. Wang, C. Shen, J. Liu, W. Zhang and S. Yao, Three-dimensional $MnCo_2O_4$/graphene composites for supercapacitor with promising electrochemical properties, *J. Alloys Compd.*, 2019, **792**, 122–129, DOI: **10.1016/j.jallcom.2019.03.405**.

33 V. H. Nguyen and J. J. Shim, Three-dimensional nickel foam/graphene/$NiCo_2O_4$ as high-performance electrodes for supercapacitors, *J. Power Sources*, 2015, **273**, 110–117, DOI: **10.1016/j.jpowsour.2014.09.031**.

34 F. Yu, *et al.*, Ultrathin $NiCo_2S_4$@graphene with a core-shell structure as a high performance positive electrode for hybrid supercapacitors, *J. Mater. Chem. A*, 2018, **6**(14), 5856–5861, DOI: **10.1039/c8ta00835c**.

35 G. Godillot, P. L. Taberna, B. Daffos, P. Simon, C. Delmas and L. Guerlou-Demourgues, High power density aqueous hybrid supercapacitor combining activated carbon and highly conductive spinel cobalt oxide, *J. Power Sources*, 2016, **331**, 277–284, DOI: **10.1016/j.jpowsour.2016.09.035**.

36 S. Silambarasan and T. Maiyalagan, Nitrogen-doped porous carbon coated on $MnCo_2O_4$ nanospheres as electrode materials for high-performance asymmetric supercapacitors, *Mater. Today Chem.*, 2023, **27**, 101350, DOI: **10.1016/j.mtchem.2022.101350**.

37 M. Sivakumar, *et al.*, Flower-like $NiCo_2O_4$ nanoflake surface covered on carbon nanolayer for high-performance electro-oxidation of non-enzymatic glucose biosensor, *Mater. Today Chem.*, 2022, **26**, 101156, DOI: **10.1016/j.mtchem.2022.101156**.

38 W. Guo, *et al.*, A Novel CVD Growth of g-C_3N_4 Ultrathin Film on $NiCo_2O_4$ Nanoneedles/Carbon Cloth as Integrated Electrodes for Supercapacitors, *ChemElectroChem*, 2018, **5**(22), 3383–3390, DOI: **10.1002/celc.201801045**.

39 Q. Y. Shan, B. Guan, J. M. Zhang, F. Dong, X. Y. Liu and Y. X. Zhang, Facile Fabrication of $NiCo_2O_4$ @g-C_3N_4 (C) Hybrids for High-Performance Supercapacitors, *J. Nanosci. Nanotechnol.*, 2018, **19**(1), 73–80, DOI: **10.1166/jnn.2019.16441**.

40 Q. Zhou, T. Fan, Y. Li, D. Chen, S. Liu and X. Li, Hollow–structure NiCo hydroxide/carbon nanotube composite for high–performance supercapacitors, *J. Power Sources*, 2019,

426(February), 111–115, DOI: **10.1016/j.jpowsour.2019.04.035**.

41 Y. Chen, X. Guo, A. Liu, H. Zhu and T. Ma, Recent progress in biomass-derived carbon materials used for secondary batteries, *Sustain. Energy Fuels*, 2021, **5**(12), 3017–3038, DOI: **10.1039/d1se00265a**.

42 J. G. Ruiz-Montoya, L. V. Quispe-Garrido, J. C. Calderón Gómez, A. M. Baena-Moncada and J. M. Gonçalves, Recent progress in and prospects for supercapacitor materials based on metal oxide or hydroxide/biomass-derived carbon composites, *Sustain. Energy Fuels*, 2021, **5**(21), 5332–5365, DOI: **10.1039/d1se01170g**.

43 S. Unknown, P. Chand and A. Joshi, Biomass derived carbon for supercapacitor applications: review, *J. Energy Storage*, 2021, **39**(January), 102646, DOI: **10.1016/j.est.2021.102646**.

44 X. Q. Lin, N. Yang, L. Qiu-Feng and R. Liu, Self-Nitrogen-Doped Porous Biocarbon from Watermelon Rind: A High-Performance Supercapacitor Electrode and Its Improved Electrochemical Performance Using Redox Additive Electrolyte, *Energy Technol.*, 2019, **7**(3), DOI: **10.1002/ente.201800628**.

45 N. F. Sylla, *et al.*, Effect of porosity enhancing agents on the electrochemical performance of high-energy ultracapacitor electrodes derived from peanut shell waste, *Sci. Rep.*, 2019, **9**(1), 1–15, DOI: **10.1038/s41598-019-50189-x**.

46 M. Biswal, A. Banerjee, M. Deo and S. Ogale, From dead leaves to high energy density supercapacitors, *Energy Environ. Sci.*, 2013, **6**(4), 1249–1259, DOI: **10.1039/c3ee22325f**.

47 M. B. Wu, *et al.*, Template-free preparation of mesoporous carbon from rice husks for use in supercapacitors, *New Carbon Mater.*, 2015, **30**(5), 471–475, DOI: **10.1016/S1872-5805(15)60201-3**.

48 N. Zhao, L. Deng, D. Luo and P. Zhang, One-step fabrication of biomass-derived hierarchically porous carbon/MnO nanosheets composites for symmetric hybrid supercapacitor, *Appl. Surf. Sci.*, 2020, **526**(March), 146696, DOI: **10.1016/j.apsusc.2020.146696**.

49 F. Yang, J. Chu, Y. Cheng, J. Gong, X. Wang and S. Xiong, Hydrothermal Synthesis of NiCo-layered Double Hydroxide Nanosheets Decorated on Biomass Carbon Skeleton for High Performance Supercapacitor, *Chem. Res. Chin. Univ.*, 2021, **37**(3), 772–777, DOI: **10.1007/s40242-020-0333-6**.

50 G. Yang and S. J. Park, Nanoflower-like NiCo2O4 grown on biomass carbon coated nickel foam for asymmetric supercapacitor, *J. Alloys Compd.*, 2020, **835**, 155270, DOI: **10.1016/j.jallcom.2020.155270**.

51 S. Liu, *et al.*, Flexible and porous Co_3O_4-carbon nanofibers as binder-free electrodes for supercapacitors, *Adv. Compos. Hybrid Mater.*, 2021, **4**(4), 1367–1383, DOI: **10.1007/s42114-021-00344-8**.

52 J. Nan, Y. Shi, Z. Xiang, S. Wang, J. Yang and B. Zhang, Ultrathin $NiCo_2O_4$ nanosheets assembled on biomass-derived carbon microsheets with polydopamine for high-performance hybrid supercapacitors, *Electrochim. Acta*, 2019, **301**, 107–116, DOI: **10.1016/j.electacta.2019.01.167**.

53 M. Kundu, G. Karunakaran and D. Kuznetsov, Green synthesis of NiO nanostructured materials using Hydrangea paniculata flower extracts and their efficient application as supercapacitor electrodes, *Powder Technol.*, 2017, **311**(3), 132–136, DOI: **10.1016/j.powtec.2017.01.085**.

54 O. E. Fadeyi, G. A. Olatunji and V. A. Ogundele, Isolation and Characterization of the Chemical Constituents of Anacardium occidentale Cracked Bark, *Nat. Prod. Chem. Res.*, 2015, **03**(05), 58–63, DOI: **10.4172/2329-6836.1000192**.

55 C. Eliakim-Ikechukwu, A. Obri and O. Akpa, Phytochemical and Micronutrient Composition of Anacardium Occidentale Linn (cashew) stem-bark hydroethanolic extract and its effect on the fasting blood glucose levels and body weight of diabetic Wistar rats, *Internet J. Nutr. Wellness*, 2009, **10**(1), 1–6, DOI: **10.5580/6ef**.

56 R. C. M. De Paula, F. Heatley and P. M. Budd, Characterization of anacardium occidentale exudate polysaccharide, *Polym. Int.*, 1998, **45**(1), 27–35, DOI: **10.1002/(SICI)1097-0126(199801)45:1<27::AID-PI900>3.0.CO;2-9**.

57 X. Han, X. Gui, T. F. Yi, Y. Li and C. Yue, Recent progress of NiCo$_2$O$_4$-based anodes for high-performance lithium-ion batteries, *Curr. Opin. Solid State Mater. Sci.*, 2018, **22**(4), 109–126, DOI: **10.1016/j.cossms.2018.05.005**.

58 M. Arunkumar and A. Paul, Importance of Electrode Preparation Methodologies in Supercapacitor Applications, *ACS Omega*, 2017, **2**(11), 8039–8050, DOI: **10.1021/acsomega.7b01275**.

59 B. Saravanakumar, T. Priyadharshini, G. Ravi, V. Ganesh, A. Sakunthala and R. Yuvakkumar, Hydrothermal synthesis of spherical NiCO$_2$O$_4$ nanoparticles as a positive electrode for pseudocapacitor applications, *J. Sol-Gel Sci. Technol.*, 2017, **84**(2), 297–305, DOI: **10.1007/s10971-017-4504-y**.

60 D. Guragain, C. Zequine, T. Poudel, D. Neupane, R. K. Gupta and S. R. Mishra, Influence of Urea on the Synthesis of NiCo$_2$O$_4$ Nanostructure: Morphological and Electrochemical Studies, *J. Nanosci. Nanotechnol.*, 2019, **20**(4), 2526–2537, DOI: **10.1166/jnn.2020.17366**.

61 J. Pan, J. Du, Y. Sun, P. Wan, X. Liu and Y. Yang, The change of structure and electrochemical property in the synthesis process of spherical NiOOH, *Electrochim. Acta*, 2009, **54**(14), 3812–3818, DOI: **10.1016/j.electacta.2009.01.083**.

62 R. P. Putra, I. B. Rachman, H. Horino and I. I. Rzeznicka, γ-NiOOH electrocatalyst derived from a nickel dithiooxamide chelate polymer for oxygen evolution reaction in alkaline solutions, *Catal. Today*, 2022, **397–399**(April), 308–315, DOI: **10.1016/j.cattod.2021.08.017**.

63 P. Zhang, X. Deng, W. Li, Z. Ma and X. Wang, Electrochemical-induced surface reconstruction to NiFe-LDHs-based heterostructure as novel positive electrode for supercapacitors with enhanced performance in neutral electrolyte, *Chem. Eng. J.*, 2022, **449**(July), 137886, DOI: **10.1016/j.cej.2022.137886**.

64 G. Ma, W. Tang, K. Sun, Z. Zhang, E. Feng and Z. Lei, Coprinus comatus-based nitrogen-doped active carbon for high performance supercapacitor, *Nano*, 2017, **12**(8), 1–15, DOI: **10.1142/S179329201750103X**.

65 A. Maghsoumi, L. Brambilla, C. Castiglioni, K. Müllen and M. Tommasini, Overtone and combination features of G and D peaks in resonance Raman spectroscopy of the C$_{78}$H$_{26}$ polycyclic aromatic hydrocarbon, *J. Raman Spectrosc.*, 2015, **46**(9), 757–764, DOI: **10.1002/jrs.4717**.

66 M. N. Iliev, *et al.*, Raman studies of cation distribution and thermal stability of epitaxial spinel NiCo$_2$O$_4$ films, *J. Appl. Phys.*, 2013, **114**(3), DOI: **10.1063/1.4815874**.

67 S. G. Krishnan, *et al.*, Critical influence of reduced graphene oxide mediated binding of M (M = Mg, Mn) with Co ions, chemical stability and charge storability enhancements of spinal-type hierarchical MCo$_2$O$_4$ nanostructures, *Electrochim. Acta*, 2017, **243**, 119–128, DOI: **10.1016/j.electacta.2017.05.064**.

68 V. Venkatachalam, A. Alsalme, A. Alghamdi and R. Jayavel, High performance electrochemical capacitor based on MnCo$_2$O$_4$ nanostructured electrode, *J. Electroanal. Chem.*, 2015, **756**, 94–100, DOI: **10.1016/j.jelechem.2015.08.019**.

69 R. H. H. Ibrahim, L. I. Darvell, J. M. Jones and A. Williams, Physicochemical characterisation of torrefied biomass, *J. Anal. Appl. Pyrolysis*, 2013, **103**, 21–30, DOI: **10.1016/j.jaap.2012.10.004**.

70 X. Yan, H. You, W. Liu, X. Wang and D. Wu, Free-standing and heteroatoms-doped carbon nanofiber networks as a binder-free flexible electrode for high-performance supercapacitors, *Nanomaterials*, 2019, **9**(9), DOI: **10.3390/nano9091189**.

71 B. Li, *et al.*, Nitrogen-doped activated carbon for a high energy hybrid supercapacitor, *Energy Environ. Sci.*, 2016, **9**(1), 102–106, DOI: **10.1039/c5ee03149d**.

72 V. Kuzmenko, *et al.*, Cellulose-derived carbon nanofibers/graphene composite electrodes for powerful compact supercapacitors, *RSC Adv.*, 2017, **7**(73), 45968–45977, DOI: **10.1039/c7ra07533b**.

73 S. Liu, D. Ni, H. F. Li, K. N. Hui, C. Y. Ouyang and S. C. Jun, Effect of cation substitution on the pseudocapacitive performance of spinel cobaltite MCo2O4 (M = Mn, Ni, Cu, and Co), *J. Mater. Chem. A*, 2018, **6**(23), 10674–10685, DOI: **10.1039/c8ta00540k**.

74 Y. Dong, *et al.*, Facile synthesis of hierarchical nanocage MnCo$_2$O$_4$ for high performance supercapacitor, *Electrochim. Acta*, 2017, **225**, 39–46, DOI: **10.1016/j.electacta.2016.12.109**.

75 D. Zhao, X. Wu and C. Guo, Hybrid MnO$_2$@NiCo$_2$O$_4$ nanosheets for high performance asymmetric supercapacitors, *Inorg. Chem. Front.*, 2018, **5**(6), 1378–1385, DOI: **10.1039/c8qi00170g**.

76 N. M. Ndiaye, M. J. Madito, B. D. Ngom, T. M. Masikhwa, A. A. Mirghni and N. Manyala, High-performance asymmetric supercapacitor based on vanadium dioxide and carbonized iron-polyaniline electrodes, *AIP Adv.*, 2019, **9**(5), DOI: **10.1063/1.5091799**.

77 H. Wang, *et al.*, Graphene-nickel cobaltite nanocomposite asymmetrical supercapacitor with commercial level mass loading, *Nano Res.*, 2012, **5**(9), 605–617, DOI: **10.1007/s12274-012-0246-x**.

78 J. Bhagwan, G. Nagaraju, B. Ramulu, S. C. Sekhar and J. S. Yu, Rapid synthesis of hexagonal $NiCo_2O_4$ nanostructures for high-performance asymmetric supercapacitors, *Electrochim. Acta*, 2019, **299**, 509–517, DOI: **10.1016/j.electacta.2018.12.174**.

79 N. M. Ndiaye, *et al.*, Effect of growth time on solvothermal synthesis of vanadium dioxide for electrochemical supercapacitor application, *Mater. Chem. Phys.*, 2018, **214**, 192–200, DOI: **10.1016/j.matchemphys.2018.04.087**.

80 B. Pal, S. Yang, S. Ramesh, V. Thangadurai and R. Jose, Electrolyte selection for supercapacitive devices: a critical review, *Nanoscale Adv.*, 2019, **1**(10), 3807–3835, DOI: **10.1039/c9na00374f**.

81 C. Zhong, Y. Deng, W. Hu, J. Qiao, L. Zhang and J. Zhang, A review of electrolyte materials and compositions for electrochemical supercapacitors, *Chem. Soc. Rev.*, 2015, **44**(21), 7484–7539, DOI: **10.1039/c5cs00303b**.

82 S. Sadavar, *et al.*, Anion storage for hybrid supercapacitor, *Mater. Today Energy.*, 2023, **37**, DOI: **10.1016/j.mtener.2023.101388**.

83 X. Lang, *et al.*, Rational design of La0.85Sr0.15MnO$_3$@NiCo$_2$O$_4$ Core–Shell architecture supported on Ni foam for high performance supercapacitors, *J. Power Sources*, 2018, **402**(September), 213–220, DOI: **10.1016/j.jpowsour.2018.09.040**.

84 X. Sun, J. Sun, C. Wu, L. Guo, L. Hou and C. Yuan, Unveiling composition/crystal structure-dependent electrochemical behaviors via experiments and first-principles calculations: rock-salt $NiCoO_2$ vs. spinel $Ni_{1.5}Co_{1.5}O_4$, *Mater. Today Energy*, 2021, **19**, 1–8, DOI: **10.1016/j.mtener.2020.100592**.

85 L. Halder, *et al.*, High performance advanced asymmetric supercapacitor based on ultrathin and mesoporous $MnCo_2O_{4.5}$-$NiCo_2O_4$ hybrid and iron oxide decorated reduced graphene oxide electrode materials, *Electrochim. Acta*, 2018, **283**, 438–447, DOI: **10.1016/j.electacta.2018.06.184**.

86 M. S. Vidhya, *et al.*, Nickel-cobalt hydroxide: a positive electrode for supercapacitor applications, *RSC Adv.*, 2020, **10**(33), 19410–19418, DOI: **10.1039/d0ra01890b**.

87 P. Hao, *et al.*, The hybrid nanostructure of $MnCo_2O_{4.5}$ nanoneedle/carbon aerogel for symmetric supercapacitors with high energy density, *Nanoscale*, 2015, **7**(34), 14401–14412, DOI: **10.1039/c5nr04421a**.

88 A. Eftekhari, On the mechanism of microporous carbon supercapacitors, *Mater. Today Chem.*, 2018, **7**, 1–4, DOI: **10.1016/j.mtchem.2017.11.004**.

89 B. Wei, H. Liang, R. Wang, D. Zhang, Z. Qi and Z. Wang, One-step synthesis of graphitic-C_3N_4/ZnS composites for enhanced supercapacitor performance, *J. Energy Chem.*, 2018, **27**(2), 472–477, DOI: **10.1016/j.jechem.2017.11.015**.

90 Y. Ren, *et al.*, Three-dimensional Al-substituted quasi-concentration gradient Ni-Co layered double hydroxide nanosheets for high-performance asymmetric supercapacitors, *Mater. Today Energy*, 2020, **18**, 1–9, DOI: **10.1016/j.mtener.2020.100514**.